Noncontact Measurement of the Instantaneous Heart Rate in a Multi-person Scenario Using X-band Array Radar and Adaptive Array Processing

Takuya Sakamoto, Senior Member, IEEE, Pascal J. Aubry, Shigeaki Okumura, Student Member, IEEE, Hirofumi Taki, Member, IEEE, Toru Sato, Member, IEEE, Alexander G. Yarovoy, Fellow, IEEE

Abstract—A noncontact measurement of the heart rate of a specific person using an X-band radar system with a four-element antenna array is presented. The system comprises a two-dimensional planar wide-beam antenna array with a four-channel network analyzer. The direction of arrival is estimated using the Capon method, and the directionally constrained minimization-of-power algorithm is then applied to the received signals. Signals from the four channels are adaptively combined to enhance the accuracy in estimating the instantaneous heart rate in a multi-person scenario. Measurement results indicate that the proposed system with the adaptive array processing technique is effective for the noncontact measurement of the heart rate of a specific person when there are more than one person in the scene.

Index Terms—microwave, radar, heart rate, adaptive array

I. Introduction

NONCONTACT measurement of heartbeats has been of great importance to a variety of health care applications because it allows long-term monitoring without uncomfortable electrodes or sensors being attached to the body. There have been numerous reports on the radar-based monitoring of vital signs covering a wide range of topics, such as circuits, antennas, system designs, measurement settings and signal processing algorithms [1]-[12]. Most of the cited studies used a monostatic radar that has only a single channel with only a pair of (transmitting and receiving) antennas. Such systems therefore need to use a wide beam to cover the test subject, who may not

T. Sakamoto is with the Department of Electrical Engineering, University of Hawaii at Manoa, 2540 Dole Street, Honolulu, HI 96822 USA, and also with the Graduate School of Engineering, University of Hyogo, 2167 Shosha, Himeji, Hyogo 671-2280, Japan, and the Graduate School of Informatics, Kyoto University, Yoshida-Honmachi, Sakyo-ku, Kyoto 606-8501, Japan.

P. J. Aubry and A. G. Yarovoy are with Microwave Sensing, Signals and Systems (MS3), Department of Microelectronics, Delft University of Technology, Delft, The Netherlands.

S. Okumura and T. Sato are with the Graduate School of Informatics, Kyoto University, Yoshida-Honmachi, Sakyo-ku, Kyoto 606-8501, Japan.

H. Taki is with the Graduate School of Biomedical Engineering, Tohoku University, 2-1 Seiryo-machi, Aoba-ku, Sendai, Miyagi 980-8575, Japan.

necessarily be in the beam mainlobe, and suffer from weak echoes returning from targets and compromised accuracy. Moreover, conventional single-channel radar systems cannot separate interfering echoes if there are multiple people in the same range bin. The measurement of vital signs of multiple people is still a challenge in this field.

Adib et al. [13] demonstrated the measurement of the vital signs of eight people using an ultra-wideband radar. In their study, however, the participants lined up along a straight line in the range direction instead of the cross-range direction. Vergara et al. [14] measured the motion of multiple body parts (the hand and torso) of a single person using a blind source separation algorithm and a single-antenna radar. Mikhelson et al. [15] built a system with a single directional antenna that can mechanically track the target person with the assistance of a depth camera that successfully tracked a walking human and measured the vital signs. Wang et al. [16] also developed a radar with a mechanically scanning antenna for measuring vital signs.

Instead of using mechanically scanning antennas, the use of array antennas is an alternative approach realizing a simple and compact system. Li et al. [17] reviewed a system with multiple antennas that measures vital signs while suppressing body motion using two antennas measuring opposite sides of the human body. Zhou et al. [18] proposed an array-based method for detecting vital signs of multiple people, but their study only conducted simulations. Boothby et al. [19] and Hall et al. [20] introduced an antenna array for vital-sign monitoring, which had an automatic steering function that tracks the target by finding the angle with the largest phase fluctuation. Samardzija et al. [21] introduced a multiple-input multiple-output radar with two Tx and four Rx and obtained a power spectrum averaged over eight Tx-Rx pairs. Hsu et al. [22] demonstrated the measurement of vital signs of multiple subjects using a four-element phased array with a self-injection-locked radar. Mostafanezhad et al. [23] used a $2 \times 2 = 4$ receiving antenna array and applied the super-resolution MUSIC algorithm to obtain respiration information of a single person, but the method was not applied to multiple people.

As mentioned above, a variety of studies have been

conducted to measure the vital signs of multiple people. Nonetheless, there have been few publications on super-resolution adaptive array techniques employed to separate echoes from multiple people and to measure the instantaneous heart rate. In this paper, we employ the super-resolution Capon method and directionally constrained minimization of power (DCMP) algorithm and show the feasibility of an accurate measurement of a person's instantaneous heart rate when two people stand next to each other at almost the same distance from the radar. The radar has four channels with an antenna array operating in the X-band (8.4 GHz). Adaptive array processing algorithms are employed to locate and measure the heartbeat of a person of interest by automatically suppressing undesired echoes from the other person. The performance of the proposed radar system is investigated through measurements, demonstrating that we can selectively extract vital signs from a specific person even when there is another person in the scene. Because the people are almost the same distance from the radar antennas, their echoes cannot be separated even when wideband signals are employed. Moreover, we employ the topology algorithm [26], [27], [28], which is robust and accurate in estimating the instantaneous heart rate, and obtain accurate interbeat intervals of the target's heartbeat. A preliminary result of this study was presented in [29].

II. Radar Measurement System and Setup

The radar system (Fig. 1) in this study consists of a four-port network analyzer (N5242A, Agilent Technologies, CA, United States of America) and a planar wide-beam 9×9 array antenna developed by Valavan et al. [30], [31], as shown in Fig. 2. Each element of the antenna array is a square of size 14.5mm $\times$ 14.5mm. The antenna array elements have beam widths of 160° and 145° in the E- and H-planes, respectively. The array antenna elements are labeled $(1,1), (1,2), \cdots, (9,9)$, where $(1,1)$ corresponds to the lower left corner when viewing from the feeding side. The element $(5,6)$ is connected to channel 1 (ch1) and transmits continuous waves with a frequency of 8.4 GHz, which is fed by network analyzer port 1. The network analyzer is operated in the continuous-wave time mode with an intermediate frequency of 200.0 Hz, and a sampling interval of $\Delta t = 5.0$ ms. We use four of the array elements, namely ch1 $(5,6)$, ch2 $(5,5)$, ch3 $(4,5)$ and ch4 $(4,4)$, as receiving antennas (see Fig. 3, which shows the array from the feeding side). The received signals $s_1(t)$, $s_2(t)$, $s_3(t)$ and $s_4(t)$ are respectively measured as the S-matrix parameters S11, S21, S31 and S41 using the network analyzer, and they are sampled using a quadrature mixer to obtain in-phase (I) and quadrature (Q) signals.

We selected these four elements, $(5,6)$, $(5,5)$, $(4,5)$ and $(4,4)$, to realize a vertically sharp beam pattern to suppress echoes from lower body parts such as legs. The selected element topology has a vertical baseline length of two element gaps, which corresponds to 0.81λ, where λ is the wavelength. In addition, the array layout has
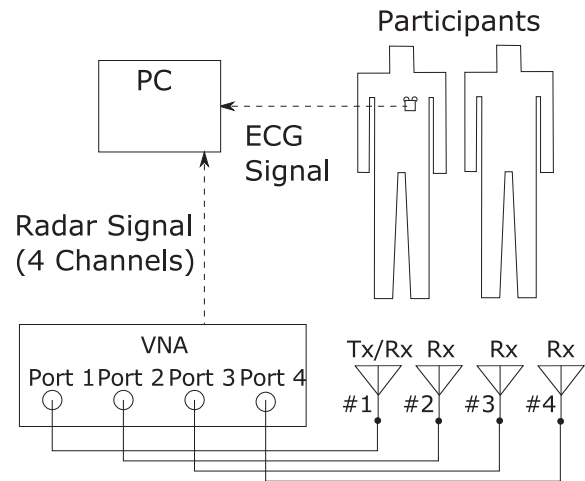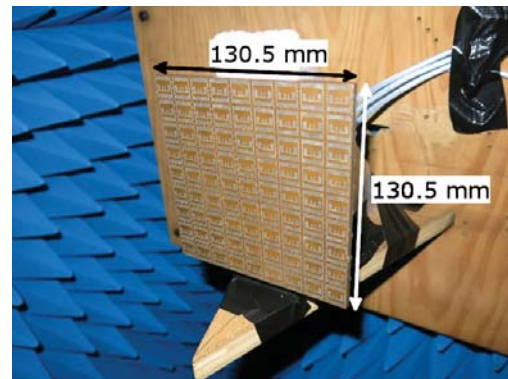

Fig. 1.   Schematic of the measurement system.

Fig. 2.   Planar 9×9 antenna array used in the present measurement.

the minimum element spacing of one element gap, which corresponds to 0.41λ, in both vertical and horizontal directions to avoid grating lobes.

The measurement was made in an anechoic chamber. Two healthy male participants (participants A and B) were instructed to stand facing the array antennas and at a distance of 0.6 m from each other. The heights of participants A and B were 178 and 174 cm, respectively. The beam width of the element pattern covered both participants. For evaluation of the accuracy in estimating the heart rate, we also made measurements using an electrocardiogram (ECG) device (RF-ECG EK, Micro Medical Device, Inc., Tokyo, Japan), which was attached to participant B. The ECG data were taken during the radar measurement. The participants were dressed normally and instructed to stand naturally at a distance of 0.5 m from the x–z plane, on which the antenna array was installed (see Fig. 4). The participants breathed normally throughout the measurement period of 50.0 s. To evaluate the performance of the proposed method, the participants were measured separately. Signals were then numerically added to obtain a set of synthesized data simulating a scenario with two participants standing simultaneously.
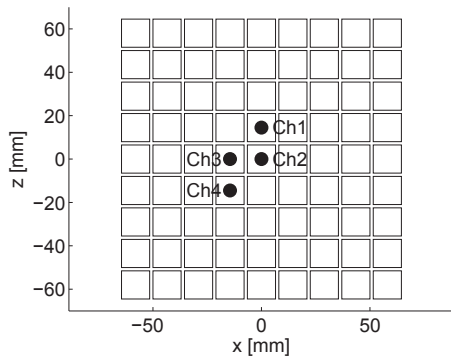
Fig. 3.   Antenna array and elements used in the measurement (as seen from the back side with feeding connectors).

Fig. 4.   Assumed measurement scenario with participants standing in front of the antenna array. The actual measurements were made separately for each participant.

III. Super-resolution Array Radar Imaging and Adaptive Array Processing

A. Signals and Preprocessing

We combine data from the four channels $s_1(t)$, $s_2(t)$, $s_3(t)$ and $s_4(t)$ using adaptive array processing, and improve the performance of estimating the instantaneous heart rate. A similar technique has been used previously [32] but for the purpose of developing a radar system that measures respiration only, while the present study aims to accurately measure the heart rate. The measurement of the heart rate is achieved in two steps: 1) locating the position of echo sources and 2) extracting the desired echo from a specific position, while suppressing undesired echoes from other directions.

Preprocessing is required before applying adaptive array processing algorithms. First, direct-current (DC) components are subtracted according to $s_i(t) = s_i^{(\mathrm{raw})}(t) - s_i^{(\mathrm{DC})}$ ($i = 1, 2, 3, 4$), where $s_i^{(\mathrm{raw})}(t)$ is a raw signal and $s_i^{(\mathrm{DC})}$ is a DC component relating to static clutter. When there is only one target, the phase of each signal varies over time because of body displacement, while the amplitude remains largely unchanged. As a result, each signal forms (part of) a circle in the complex plane, and its center corresponds to the DC interference caused by static clutter. Exploiting this prior information, most of the static

clutter (DC component) can be removed by estimating the center of the circles in the data samples. We note that the DC component can be also generated through nonlinear phase modulation of multiple interfering signals and their harmonics [33]. Although there are elaborate methods of estimating and removing the DC component when measuring vital signs [34], [35], [36], they can be applied only when there is a single dominant reflection point, which is not the case in this study. We therefore simply average the raw signal to obtain the DC component $s_i^{(\mathrm{DC})} = 1/T_0 \int_0^{T_0} s_i^{(\mathrm{raw})}(t)\mathrm{d}t$. Next, the phase of the array elements needs to be calibrated using measured echoes from a known target at a known position. We used a metallic sphere having a diameter of 20.0 cm as a target for this calibration measurement.

B. Array Beamforming

After completing the above preprocessing procedures, we actually measure echoes from human targets. We estimate the direction of arrival (DOA) of the echoes and identify the reflection locations on the bodies of participants. For this purpose, the most basic approach is beamforming imaging, in which the image $P_{\mathrm{BF}}(\theta, \phi)$ forms as

$$
\begin{aligned}
P_{\mathrm{BF}}(\theta, \phi) &= \frac{1}{T_0} \int_0^{T_0} |\boldsymbol{a}(\theta,\phi)^{\mathrm{H}} \boldsymbol{s}(t)|^2 \mathrm{d}t, \\
&= \boldsymbol{a}(\theta,\phi)^{\mathrm{H}} R_{ss} \boldsymbol{a}(\theta,\phi).
\end{aligned} \tag{1}
$$

Here $\boldsymbol{s}(t) = [s_1(t), s_2(t), s_3(t), s_4(t)]^{\mathrm{T}}$ is a signal vector consisting of signals from all channels, where superscripts T and H denote transpose and conjugate transpose operators, respectively. The correlation matrix R_{ss} is calculated as

$$
R_{ss} = \frac{1}{T_0} \int_0^{T_0} \boldsymbol{s}(t)\boldsymbol{s}^{\mathrm{H}}(t)\mathrm{d}t, \tag{2}
$$

where an ensemble average is approximated by a time average, assuming the ergodic hypothesis. Vector $\boldsymbol{a}(\theta,\phi)$ is called a steering vector or mode vector, and is given as

$$
\boldsymbol{a}(\theta,\phi) = [\boldsymbol{k} \cdot \boldsymbol{r}_1, \boldsymbol{k} \cdot \boldsymbol{r}_2, \boldsymbol{k} \cdot \boldsymbol{r}_3, \boldsymbol{k} \cdot \boldsymbol{r}_4]^{\mathrm{T}}, \tag{3}
$$

where $\boldsymbol{k}$ is a k-vector and $\boldsymbol{r}_1$, $\boldsymbol{r}_2$, $\boldsymbol{r}_3$ and $\boldsymbol{r}_4$ are the position vectors of elements 1, 2, 3 and 4, respectively. Additionally, $\boldsymbol{k}$ is expressed as a function of zenith and azimuth angles θ and ϕ:

$$
\boldsymbol{k}(\theta,\phi) = k[\sin\theta\cos\phi, \sin\theta\sin\phi, \cos\theta]^{\mathrm{T}}, \tag{4}
$$

where $k = 2\pi/\lambda$ is a scalar wavenumber. $\lambda = 3.6$ cm for a frequency of 8.4 GHz in this study. The spatial resolution of the beamforming image is restricted by the size of the antenna array; a large-scale array with a number of elements is needed to sharpen the beam pattern.

C. Capon Method

To overcome the above difficulty, we adopt the Capon method, which is known as a super-resolution DOA estimation method. Let us consider an output signal $y(t) = w_1^* s_1(t) + w_2^* s_2(t) + w_3^* s_3(t) + w_4^* s_4(t) = \boldsymbol{w}^{\mathrm{H}} \boldsymbol{s}(t)$

that is a summation of the weighted input signals from a multi-channel receiver, where superscript $*$ denotes a complex conjugate and $\boldsymbol{w} = [w_1, w_2, w_3, w_4]^{\mathrm{T}}$ is a four-dimensional complex-valued weight vector. The power of the output signal is

$$
\begin{aligned}
|y(t)|^2 &= |\boldsymbol{w}^{\mathrm{H}}\boldsymbol{s}(t)|^2 \\
&= \boldsymbol{w}^{\mathrm{H}}\boldsymbol{s}(t)(\boldsymbol{w}^{\mathrm{H}}\boldsymbol{s}(t))^{\mathrm{H}} \\
&= \boldsymbol{w}^{\mathrm{H}}\boldsymbol{s}(t)\boldsymbol{s}^{\mathrm{H}}(t)\boldsymbol{w},
\end{aligned}
\tag{5}
$$

and its expectation $\mathrm{E}[|y(t)|^2] = \boldsymbol{w}^{\mathrm{H}}R_{ss}\boldsymbol{w}$ is used in the Capon method, where superscript H is a conjugate transpose operator, $\mathrm{E}[]$ is an expectation operator, and $R_{ss} = \mathrm{E}[\boldsymbol{s}(t)\boldsymbol{s}^{\mathrm{H}}(t)]$ is a correlation matrix of the signal $\boldsymbol{s}(t)$.

The Capon spectrum $P_{\mathrm{C}}(\theta, \phi)$ is derived from the optimization problem

$$
\begin{aligned}
P_{\mathrm{C}}(\theta, \phi) = \min_{\boldsymbol{w}} \boldsymbol{w}^{\mathrm{H}}R_{ss}\boldsymbol{w}, \\
\text{subject to } \boldsymbol{w}^{\mathrm{H}}\boldsymbol{a}(\theta, \phi) = 1.
\end{aligned}
\tag{6}
$$

Equation (6) indicates that the Capon method finds the optimum weight $\boldsymbol{w}$ that minimizes the output power $\mathrm{E}[|y(t)|^2] = \boldsymbol{w}^{\mathrm{H}}R_{ss}\boldsymbol{w}$ under a condition that the gain for a specific direction (θ, ϕ) is maintained to be 1. Because we assume that each of the multiple echoes arriving from different directions has no correlation with the others, the output power is minimized by suppressing other echoes except for the echo arriving from (θ, ϕ). The system scans two-dimensionally over (θ, ϕ) in the region of interest to generate the Capon spectrum used for DOA estimation. The value of each pixel of the Capon spectrum image corresponds to the total power of the output signal $\mathrm{E}[|y(t)|^2]$.

The solution to the optimization problem (Eq. (6)) for $\boldsymbol{w}$ is obtained as a Wiener solution, and the resultant image $P_{\mathrm{C}}(\theta, \phi)$ is given by

$$
P_{\mathrm{C}}(\theta, \phi) = \frac{1}{\boldsymbol{a}^{\mathrm{H}}(\theta, \phi)(R_{ss} + \epsilon I)^{-1}\boldsymbol{a}(\theta, \phi)},
\tag{7}
$$

where I is an identity matrix and an unimportant constant is neglected. In Eq. (7), ϵ is called a diagonal loading value. A small diagonal loading value enhances the spatial resolution, whereas a large value makes the imaging process robust. In this study, the diagonal loading is set to be proportional to the summation of the average power of each channel: $\epsilon = \epsilon_0 \mathrm{tr}(R_{ss})$, where $\mathrm{tr}(\cdot)$ denotes a trace of a matrix. By searching for the dominant peaks of $P_{\mathrm{C}}(\theta, \phi)$, the DOA θ_0 and ϕ_0 of echoes can be determined.

D. Directionally Constrained Minimization of Power

We next use the directionally constrained minimization of power (DCMP) algorithm to extract the echo from the estimated DOA (θ_0, ϕ_0), while suppressing signals and clutter from other directions. This algorithm is similar to the Capon method, and the problem is formulated as

$$
\begin{aligned}
\boldsymbol{w}_{\mathrm{opt}} = \arg\min_{\boldsymbol{w}} \boldsymbol{w}^{\mathrm{H}}R_{ss}\boldsymbol{w}, \\
\text{subject to } \boldsymbol{w}^{\mathrm{H}}\boldsymbol{a}_0 = 1,
\end{aligned}
\tag{8}
$$

where $\boldsymbol{w}$ is a weight vector and $\boldsymbol{a}_0$ is defined as $\boldsymbol{a}_0 = \boldsymbol{a}(\theta_0, \phi_0)$, with θ_0 and ϕ_0 being the DOA found in the Capon spectrum as $\arg\max_{\theta, \phi} P_{\mathrm{C}}(\theta, \phi)$.

The Lagrange multiplier method [24] is used to solve the optimization problem in Eq. (8) by minimizing the Lagrangian L as

$$
\begin{aligned}
L(\boldsymbol{w}, \lambda_0) &= \tfrac{1}{2}\boldsymbol{w}^{\mathrm{H}}R_{ss}\boldsymbol{w} + \mathrm{Re}[\lambda_0(\boldsymbol{w}^{\mathrm{H}}\boldsymbol{a}_0 - 1)] \\
&= \tfrac{1}{2}\boldsymbol{w}^{\mathrm{H}}R_{ss}\boldsymbol{w} + \tfrac{1}{2}\lambda_0(\boldsymbol{w}^{\mathrm{H}}\boldsymbol{a}_0 - 1) \\
&\quad + \tfrac{1}{2}\lambda_0^*(\boldsymbol{w}^{\mathrm{T}}\boldsymbol{a}_0^* - 1),
\end{aligned}
\tag{9}
$$

where λ_0 is called a Lagrange multiplier. The gradient of $L(\boldsymbol{w}, \lambda_0)$ in terms of $\boldsymbol{w}$ must be zero;

$$
\nabla_{\boldsymbol{w}}L(\boldsymbol{w}, \lambda_0) = R_{ss}\boldsymbol{w} + \lambda_0\boldsymbol{a}_0 = 0.
\tag{10}
$$

Weight $\boldsymbol{w}$ satisfying Eq. (10) is therefore

$$
\boldsymbol{w} = -\lambda_0 R_{ss}^{-1}\boldsymbol{a}_0,
\tag{11}
$$

where we assume R_{ss} is a matrix of full rank. By substituting Eq. (11) into the constraint of Eq. (8), we obtain

$$
\lambda_0 = -\frac{1}{\boldsymbol{a}_0^{\mathrm{H}}R_{ss}^{-1}\boldsymbol{a}_0}.
\tag{12}
$$

By substituting Eq. (12) into Eq. (11), we obtain

$$
\boldsymbol{w} = \frac{R_{ss}^{-1}\boldsymbol{a}_0}{\boldsymbol{a}_0^{\mathrm{H}}R_{ss}^{-1}\boldsymbol{a}_0}.
\tag{13}
$$

In the derivation of $\boldsymbol{w}$ above, we assumed the full rankness of R_{ss}, which is not always true. When R_{ss} is close to a singular matrix, the calculation R_{ss}^{-1} becomes inaccurate, leading to an unreliable beam pattern. To avoid this problem, we use the idea of the tamed adaptive antenna array [25] and obtain the optimum weight as

$$
\boldsymbol{w}_{\mathrm{opt}} = \frac{(R_{ss} + \epsilon'I)^{-1}\boldsymbol{a}_0}{\boldsymbol{a}_0^{\mathrm{H}}(R_{ss} + \epsilon'I)^{-1}\boldsymbol{a}_0}.
\tag{14}
$$

The output of the DCMP algorithm $s_{\mathrm{DCMP}}(t)$ is thus

$$
s_{\mathrm{DCMP}}(t) = \boldsymbol{w}_{\mathrm{opt}}^{\mathrm{H}}\boldsymbol{s}(t).
\tag{15}
$$

The diagonal loading value $\epsilon' = \epsilon_0' \mathrm{tr}(R_{ss})$ can be selected independently of the Capon method's diagonal loading value ϵ.

We here explain the principle of the DCMP for rejecting interference with a simple example. The optimization problem Eq. (8) is to find a weight that minimizes the power of the output signal $\boldsymbol{w}^{\mathrm{H}}\boldsymbol{s}(t)$. The output signal contains the desired echo $s_{\mathrm{d}}(t)$ arriving from DOA (θ_0, ϕ_0) as well as the interference echo $s_{\mathrm{i}}(t)$ arriving from DOA $(\theta_{\mathrm{i}}, \phi_{\mathrm{i}})$. To simplify the discussion in this paragraph, we assume only two echoes (i.e., the desired and interference echoes) and further assume that they have no correlation. The antenna gain for the desired echo is constrained as $G(\theta_0, \phi_0) = 1$, and the gain $G(\theta_{\mathrm{i}}, \phi_{\mathrm{i}}) = |\alpha(\boldsymbol{w})|^2$ depends on the weight $\boldsymbol{w}$, where $\alpha(\boldsymbol{w})$ is an array factor in the direction $(\theta_{\mathrm{i}}, \phi_{\mathrm{i}})$. The output signal is written as $\boldsymbol{w}^{\mathrm{H}}\boldsymbol{s}(t) = s_{\mathrm{d}}(t) + \alpha(\boldsymbol{w})s_{\mathrm{i}}(t)$, and its power expectation $\mathrm{E}[|s_{\mathrm{d}}(t) + \alpha(\boldsymbol{w})s_{\mathrm{i}}(t)|^2] = \mathrm{E}[|s_{\mathrm{d}}(t)|^2] + |\alpha(\boldsymbol{w})|^2\mathrm{E}[|s_{\mathrm{i}}(t)|^2]$ is always larger than the power of the desired echo $|s_{\mathrm{d}}(t)|^2$. Thus, by minimizing the output power by adjusting the

weight $\boldsymbol{w}$, we can automatically find a small $|\alpha(\boldsymbol{w})|$ and the interference echo $s_{\mathrm{i}}(t)$ is rejected. This is the principle of the use of the DCMP to obtain the echo from a specific participant in this study.

Ideally, the signal $s_{\mathrm{DCMP}}(t)$ only contains the echo from a target at a specific DOA (θ_0, ϕ_0), and the vital signs of a specific participant can thus be obtained. Because $s_{\mathrm{DCMP}}(t)$ ideally contains an echo from a single target only, the displacement of the target can be obtained simply by calculating the phase $\angle s_{\mathrm{DCMP}}(t)$ and applying an unwrapping process assuming continuity in the phase change over time. We finally apply the topology algorithm [26], [27], [28] to the displacement time series and obtain the interbeat interval and instantaneous heart rate. The topology algorithm exploits the state transition of heartbeat waveforms, and extracts feature points from the displacement time series. The topological similarity between two adjacent heartbeats is effectively used to estimate the instantaneous heart rate and interbeat interval. The outstanding accuracy of the topology algorithm has been demonstrated in previous studies [26], [27], [28].

IV. Beamforming and Capon Method for the Imaging of Human Bodies

We first measure each participant standing alone in front of the antenna array (see Fig. 5). Participants A and B were instructed to stand facing the x–z plane at $(x, y) = (-0.3\mathrm{m}, 0.5\mathrm{m})$ (participant A) and $(x, y) = (0.3\mathrm{m}, 0.5\mathrm{m})$ (participant B). Thus, when synthesizing the echo signals from both participants, the distance between the participants is 0.6 m. The measured signals for participants A and B are respectively denoted $\boldsymbol{s}_{\mathrm{A}}(t)$ and $\boldsymbol{s}_{\mathrm{B}}(t)$.

Figure 6 shows the images generated by beamforming processing with the four-channel signals for participants A (top) and B (bottom). Because the layout of the four-channel array is asymmetric, the resultant beam spot is not symmetric vertically or horizontally, and an inclined beam spot is seen in Fig. 6. The peak of each image is located approximately at the center of the upper torso, although the spatial resolution is not high.

The upper and lower images in Fig. 7 are a photograph of the assumed scenario with two participants standing, and the beamforming image obtained using the synthesized signals $\boldsymbol{s}_{\mathrm{A}}(t) + \boldsymbol{s}_{\mathrm{B}}(t)$. We note that the synthesized signals are the summation of the two measured signals $\boldsymbol{s}_{\mathrm{A}}(t)$ and $\boldsymbol{s}_{\mathrm{B}}(t)$. In the lower image, the participants' bodies cannot be separated from each other because multiple echoes from the bodies interfere with each other. The operating frequency of 8.4 GHz corresponds to a wavelength $\lambda = 35.7$ mm, and the array aperture has a height of 29.0 mm (0.81 λ) and width of 14.5 mm (0.41 λ). When applying a conventional beamforming method, the array aperture results in beam widths of 62.7° and 123.9° in the E- and H-planes, respectively. Because the human targets are located at 0.5 m from the x–z plane (or $y = 0.5$ m), the vertical and horizontal beam spot sizes are 0.55 and 1.1 m, which are not small enough

Fig. 5. Measurement scenarios with participants A and B standing in front of the antenna array.

to resolve the two people horizontally separated by 0.6 m. It is thus concluded that conventional beamforming imaging does not provide sufficient spatial resolution in our measurement setting.

To obtain an image with higher resolution, we apply the Capon method to the synthesized signals $\boldsymbol{s}_{\mathrm{A}}(t) + \boldsymbol{s}_{\mathrm{B}}(t)$, and obtain an image as shown in Fig. 8. Here, we set diagonal loading value $\epsilon_0 = 10^{-5}$ in the Capon method. In general, by using a small diagonal loading value, the Capon method can generate a high-resolution Capon spectrum image as long as the signal-to-noise ratio is high. In this image, we see two peaks corresponding to the two target human bodies. Because the degree of freedom of the antenna array is not large enough, the peaks are not accurately located at the actual positions of the target bodies. Nevertheless, the resulting image indicates that there are two dominant targets in the scene. In Fig. 8, the peak for participant B is located at $(x, z) = (28.9\mathrm{cm}, -0.8\mathrm{cm})$. By detecting the peak corresponding to participant B, we obtain the DOA (θ_0, ϕ_0) and the mode vector $\boldsymbol{a}_0$, which is used in the DCMP algorithm.

V. Retrieval of the Desired Echo from a Specific Person Using an Adaptive Array

A. Application to a Single Human Target

A single-person scenario is first considered for simplicity. Figure 9 shows the normalized complex signals $\boldsymbol{s}_{\mathrm{B}}(t)$ with biases $-1 - \mathrm{j}$, $1 - \mathrm{j}$, $-1 + \mathrm{j}$ and $1 + \mathrm{j}$ for channels 1, 2, 3 and 4, respectively, such that the signal trajectories are displayed clearly. As explained in the previous section, the signals $\boldsymbol{s}_{\mathrm{B}}(t)$ have been preprocessed, which means that
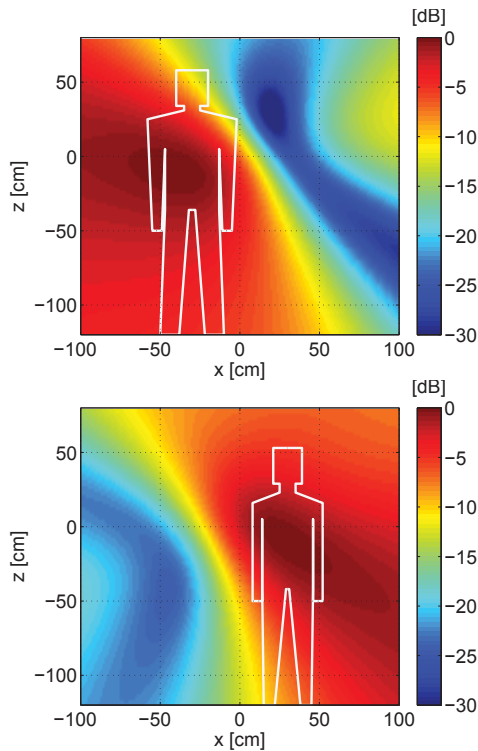
This article has been accepted for publication in a future issue of this journal, but has not been fully edited. Content may change prior to final publication. Citation information: DOI 10.1109/JETCAS.2018.2809582, IEEE Journal on Emerging and Selected Topics in Circuits and Systems

6

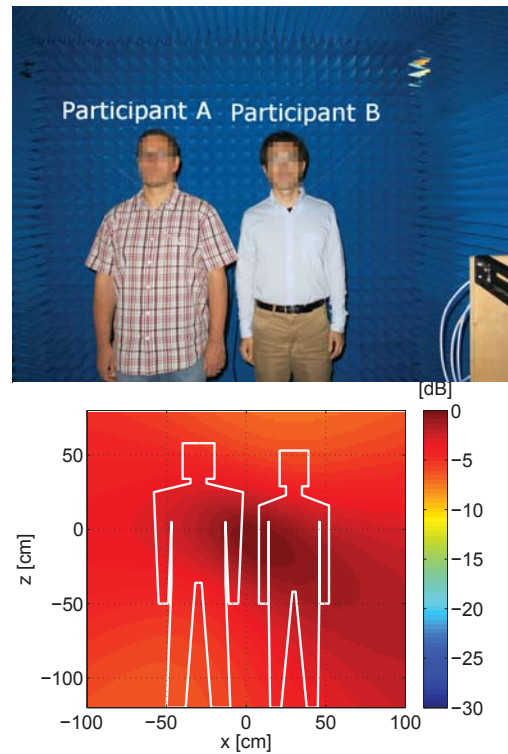Fig. 6. Beamforming images of participants A (top) and B (bottom).

Fig. 7. Assumed scenario with two participants standing (top) and beamforming image obtained from the synthesized echoes of participants A and B (bottom).

the DC components have been removed and the phase of each channel has been calibrated. Only participant B stands in front of the antenna array in this scenario. The signals exhibit a round and circle-like shape (see Fig. 9). If there is only a single scattering center (or reflection point) that has a displacement of a few centimeters and is located half a meter from the antennas, the complex echo trajectory can be approximated as a circle or part of a circle. This is because the echo intensity is not as sensitive as the echo phase to the small displacement.

We calculate the correlation matrix R_{ss} from $\boldsymbol{s}_{\mathrm{B}}(t)$, apply the DCMP algorithm to R_{ss} and obtain the optimum weight vector $\boldsymbol{w}_{\mathrm{opt}}$ according to Eq. (15) using mode vector $\boldsymbol{a}_0$ obtained in the previous section. The resultant antenna pattern is given by

$$P_{\mathrm{DCMP}}(\theta, \phi) = \boldsymbol{w}_{\mathrm{opt}}^{\mathrm{H}} \boldsymbol{a}(\theta, \phi) \qquad (16)$$

and is shown in Fig. 10. Here, the diagonal loading value $\epsilon'_0 = 0.1$ is selected. We selected a larger diagonal loading value for the DCMP than for the Capon method. This is because if a small diagonal loading value is used in the DCMP, the null of the beam pattern becomes too sharp for suppressing a nonstationary interference signal. The DOA of the interference can vary over time owing to the motion of the human body, and the DOA of the interference might move out of the sharp null of the beam pattern, which can lead to a larger interference level. This effect has been discussed by [32], and we selected the diagonal loading values accordingly. In the figure, the chest area is indicated with a circle and the gain of the antenna pattern in the chest area is fixed at 0 dB, while other echoes coming from
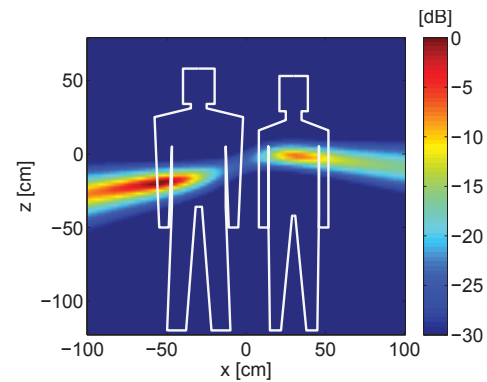

Fig. 8. Image generated by applying the Capon method to the signal for participants A and B.

different directions are suppressed. The figure shows that a null belt forms across the legs of participant B.

The DCMP weight generates the output signal $s_{\mathrm{DCMP}}(t) = \boldsymbol{w}_{\mathrm{opt}}^{\mathrm{H}} \boldsymbol{s}_{\mathrm{B}}(t)$ by optimally combining four signals; see Fig. 11. The figure shows that the trajectory is symmetric about the origin point and more uniformly round than the signals shown in Fig. 9, which indicates that there is a single dominant reflection point within the DCMP beam.

We note that Fig. 11 shows not only phase modulation but also amplitude modulation. This amplitude modulation cannot be explained using a radar equation with a constant radar cross section $P \propto r(t)^{-4}$, where P is
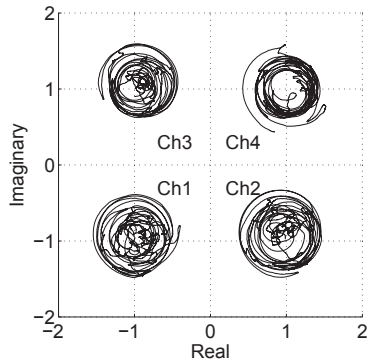
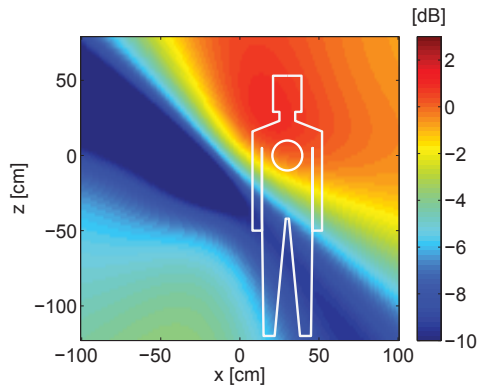Fig. 9.   Received signals $s_{\mathrm{B}}(t)$ plotted on a complex plane.

Fig. 11.   DCMP output $s_{\mathrm{DCMP}}(t)$ for participant B plotted on a complex plane.

Fig. 10.   DCMP antenna pattern for participant B.
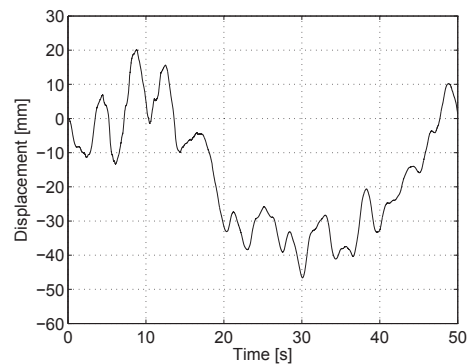
Fig. 12.   Displacement $d_{\mathrm{DCMP}}(t)$ calculated using the output of the DCMP algorithm $s_{\mathrm{DCMP}}(t)$ from signal $s_{\mathrm{B}}(t)$ for participant B.

the echo power and r is the distance to the target; the amplitude is actually modulated by the time-varying radar cross section of the human body. Because strong echoes are caused by specular reflection from a human body, even a slight change in the body orientation can affect the radar cross section as well as the echo amplitude.

We also see multiple phase rotations in the signal trajectory of Fig. 11. Because the wavelength is 35.7 mm, this phase rotation cannot be explained by typical respiration alone. A possible cause of the phase rotation is unconscious body swing. In future work, it will be important to investigate the effect of body swing in measuring the heart rates of multiple participants.

We next calculate the displacement of the target (participant B) from signals $s_1(t)$ and $s_{\mathrm{DCMP}}(t)$ for comparison. The displacement $d_{\mathrm{DCMP}}(t)$ is calculated as

$$d_{\mathrm{DCMP}}(t) = \frac{\lambda}{4\pi}\mathrm{unwrap}(\angle s_{\mathrm{DCMP}}(t)), \qquad (17)$$

where $\mathrm{unwrap}(\cdot)$ denotes an unwrapping process written as

$$\mathrm{unwrap}(\theta(t)) = \begin{cases} \theta(t) & (|\theta(t) - \theta(t - \Delta t)| \leq \pi), \\ \theta(t) + 2\pi & (\theta(t) - \theta(t - \Delta t) < -\pi), \\ \theta(t) - 2\pi & (\theta(t) - \theta(t - \Delta t) > \pi). \end{cases} \qquad (18)$$

Here, Δt is the sampling time interval of the digital signal. Note that Eq. (17) holds only when there is a

single echo from a single target, which necessitates the use of the DCMP algorithm. In a similar way, we calculate the displacement $d_1(t)$ from a single-channel signal $s_1(t)$, which would not correspond to the actual displacement of the target because the signal could contain multiple echoes.

Figure 12 shows the displacements $d_{\mathrm{DCMP}}(t)$ calculated from $\angle s_{\mathrm{DCMP}}(t)$. Figure 12 shows that the peak-to-peak displacement is approximately 65 mm; this value is the sum of multiple components, such as unconscious body swing, respiration and the heartbeat. Although the participant stands still, the upper torso is not devoid of movement.

B. Application to Multiple Human Targets

Figure 13 shows each channel of the synthesized signals $s_{\mathrm{A}}(t) + s_{\mathrm{B}}(t)$ on a complex plane. Compared with Fig. 9, the trajectories are distorted from a round circle-like shape, which indicates that multiple interfering echoes modulate the amplitude of the signals. The displacement calculated from channel 1 $s_1(t)$ of the synthesized signal $s_{\mathrm{A}}(t) + s_{\mathrm{B}}(t)$ is shown in Fig. 14. The displacement calculated from a single channel is different from the reference displacement (Fig. 12). This result indicates that a system with a single channel is not reliable when there are two
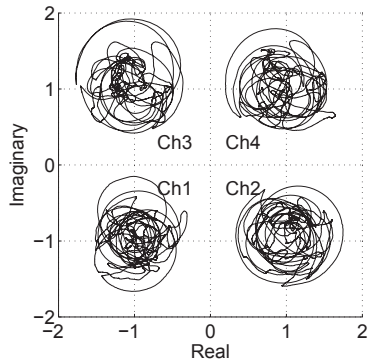
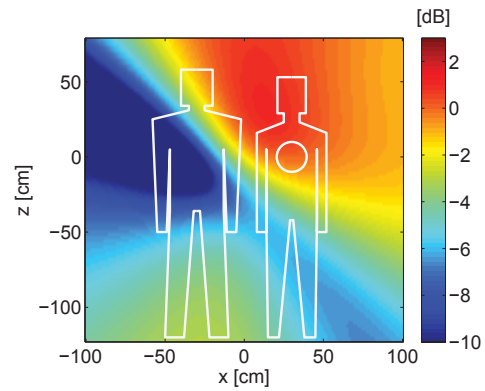Fig. 13. Received signals $s_A(t)+s_B(t)$ plotted on a complex plane.
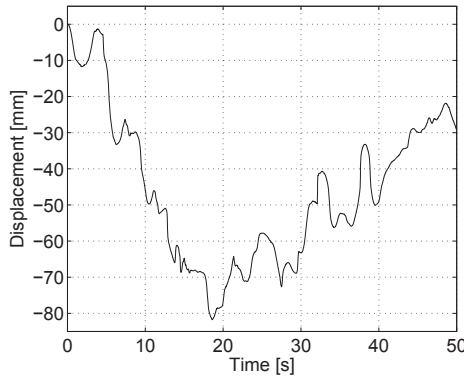

Fig. 15. DCMP antenna pattern for participants A and B.

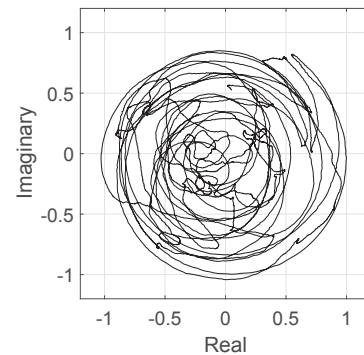Fig. 14. Displacement corresponding to the phase of channel-1 signal $s_1(t)$ for participants A and B.

Fig. 16. DCMP output s_{DCMP} calculated from echoes of participants A and B plotted on a complex plane.

or more people because of the interference of echoes that disturbs the phase and estimation of displacement.

We next apply the DCMP algorithm to the synthesized signals $s_A(t) + s_B(t)$ and selectively obtain the echo from one of the participants. Figure 15 shows the DCMP antenna pattern calculated from the correlation matrix R_{ss} and the position of participant B's chest θ_0 and ϕ_0. The figure shows that the gain for the legs of participant B is slightly raised, while a deep null band forms around the upper torso of participant A that suppresses a strong echo from him. An important point is that this beam pattern automatically forms even when we do not know the position of the source of interference (participant A) as long as we know the position of the desired echo (participant B). The DCMP algorithm optimizes the antenna pattern only using the correlation matrix of the multi-channel signals.

We finally apply the DCMP algorithm and obtain the desired echo signal from participant B, while suppressing the echo from participant A. We show the signal trajectory of $s_{DCMP}(t)$ on a complex plane (see Fig. 16). Although the trajectory slightly differs from that in Fig. 11, the shape is more symmetrical and round than that in Fig. 13, which indicates that the DCMP successfully extracted the dominant signal among multiple interfering echoes. Figure

17 shows the displacement calculated from the output of the DCMP algorithm applied to $s_A(t)+s_B(t)$. Aside from minor differences around $t = 10$ s, the displacement is successfully restored from the multi-person signals. In the next section, we extract the instantaneous heart rate from the output of the DCMP algorithm.
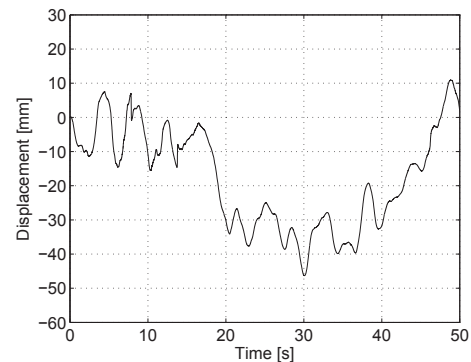

Fig. 17. Displacement $d_{DCMP}(t)$ calculated using the output of the DCMP algorithm $s_{DCMP}(t)$ from signal $s_A(t)+s_B(t)$ for participants A and B.
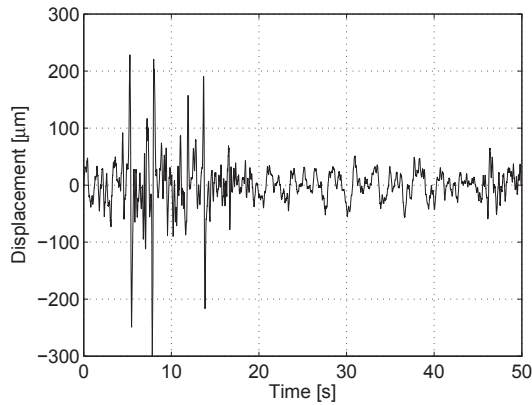
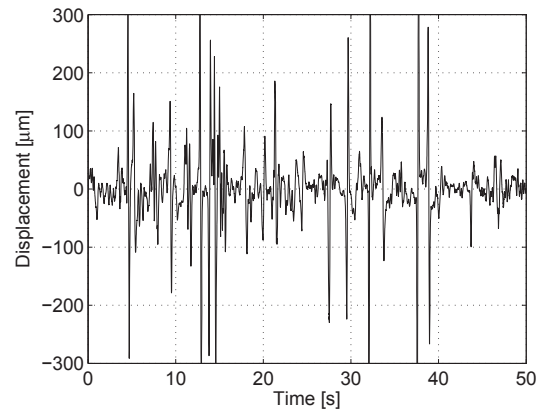Fig. 18. High-frequency component of the phase of $s_{\mathrm{DCMP}}(t)$ obtained from $\boldsymbol{s}_{\mathrm{B}}(t)$.

Fig. 19. High-frequency component of the phase of a single channel $s_1(t)$ obtained from $\boldsymbol{s}_{\mathrm{A}}(t) + \boldsymbol{s}_{\mathrm{B}}(t)$.

VI. Extraction of Displacement Associated with Vital Signs

The estimated displacement of the human target contains the body swing and respiration in addition to the heartbeat. We therefore apply a high-pass filter (HPF) to the displacement estimated from the unwrapped signal phase and extract the component associated with the heart activity. The cut-off frequency of the HPF is empirically selected to be 13.3 Hz, corresponding to 75.0 ms in the time domain. The cut-off frequency was set to be higher than the actual heartbeat frequency because the topology method is known to be effective when using high-frequency components.

We apply the HPF to the displacement obtained from the output of the DCMP algorithm when only participant B is in the scene, and obtain a high-frequency displacement (see Fig. 18). The figure shows that for 15 s $\leq t \leq$ 45 s, the amplitude is mostly smaller than 50 μm and much smaller than the wavelength. It is necessary to detect such a tiny displacement for measuring the heart rate, which requires a high signal-to-noise ratio and signal-to-interference ratio. This is the motivation of the present study and the reason why we need to introduce adaptive array processing to improve the signal-to-interference ratio in the present study. Figures 19 and 20 show the high-frequency displacements obtained from a single channel and the DCMP output, respectively, when there are both participants A and B. The coefficient of correlation between the signals in Figs. 18 and 20 for 20 s $\leq t \leq$ 40 s is 0.17, whereas the coefficient of correlation between the signals in Figs. 18 and 19 for the same time range is 0.91. This result suggests that the use of the DCMP resulted in the output signal for two participants being similar to the signal for a single participant. The displacement in Fig. 18 is considered to be associated with participant B's heart activity, and the similarity of signals in Figs. 18 and 20 suggests the effectiveness of the adaptive array processing in retrieving vital information when there are multiple people in the scene.

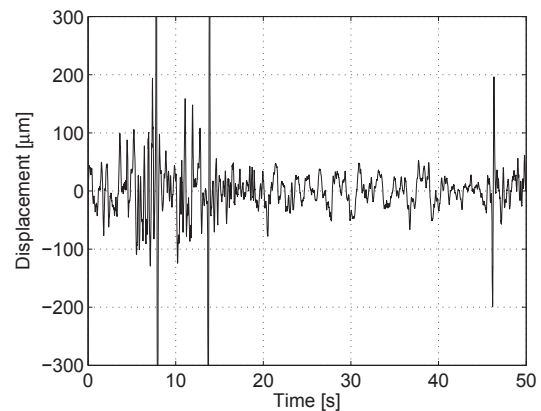We note that the amplitude of displacement in Figs. 18

Fig. 20. High-frequency component of the phase of DCMP output $s_{\mathrm{DCMP}}(t)$ obtained from $\boldsymbol{s}_{\mathrm{A}}(t) + \boldsymbol{s}_{\mathrm{B}}(t)$.

and 20 is time dependent and varies from a few tens of microns to 0.5 mm. It is known that the heart rate is not constant; it varies even within intervals of a few seconds. The instantaneous heart rate is therefore not equal to the heart rate averaged over a minute, and the actual instantaneous heart rate cannot be obtained by simply applying a Fourier transform to the displacement time series.

Instead, we apply the topology algorithm [26], which is known to be an effective method of accurately estimating the instantaneous heart rate from radar displacement data. The interbeat interval is obtained using the signals' topological features. The interbeat interval is defined as the time period between two adjacent heartbeats, which is the reciprocal of the instantaneous heart rate. In the next section, we apply the topology algorithm to the displacement time series and obtain the heart rate.

VII. Measurement of the Instantaneous Heart Rate Using an Adaptive Array

The wireless ECG device attached to participant B allows us to evaluate the accuracy of estimating the

instantaneous heart rate by comparing the estimates of the radar and ECG. We apply the topology algorithm to the high-frequency component of the displacement, where the displacement is calculated from the phase of the signal. Note that the calculated 'displacement' is accurate only when there is a single dominant echo from a single direction.

Figure 21 compares the interbeat intervals obtained from the output of the HPF and DCMP applied to $s_\mathrm{B}(t)$, assuming that only participant B is in the scene. Note that the vertical axis represents the interbeat interval, not the displacement. In the figure, the black line and red circles are the estimates made using the ECG and radar, respectively. An important point is that the proposed system and algorithms estimated not an average heart rate but an instantaneous heart rate that changes from beat to beat, which is much more difficult than merely estimating the average heart rate. The relatively high heart rate could be related to the psychological state during the measurement or the personal constitution of the participant.

Figures 22 and 23 show the interbeat intervals estimated from a single channel $s_1(t)$ and the output of DCMP $s_\mathrm{DCMP}(t)$ when both participants A and B are in the scene. To provide a comparison between different array processing techniques applied to the same number of channels, Fig. 24 shows the interbeat intervals estimated from the output of the array beamforming when both participants are in the scene. The mainlobe of the beam is directed to the DOA of the desired echo. From Figs. 21, 22 and 23, we also note that some points are missing, resulting in there being no estimates over certain periods; e.g., data points for 20–30 s are missing in Figs. 21 and 23 while data points for 25–35 s are missing in Fig. 22. This is due to the nature of the topology algorithm, which rejects unreliable estimates indicated by a low value of topology similarity between two adjacent pulses [26]. Figures 25, 26 and 27, respectively corresponding to Figs. 21, 22 and 23, show the heart rates in beats per minute (bpm) instead of the interbeat interval for convenience. Figure 28 shows the normalized histograms of errors in estimating the heart rate using DCMP for one participant and two participants, and using a single channel for two participants. The distribution of the error when using the DCMP for two participants is narrower than that when using a single channel, which indicates the effectiveness of the proposed approach using multiple channels.

We note that the measurement does not need to be repeated multiple times for the comparison of different adaptive array algorithms. This is because our receiver can measure and store all signals received by the four antenna elements; the adaptive array algorithms can be applied offline to the multiple-channel data after the measurement.

By assuming that the ECG measurements provide an accurate heart rate, we can evaluate the root-mean-square (RMS) error of each channel of the radar measurement. When there is a single participant B, the RMS errors in estimating the interbeat intervals using a single channel
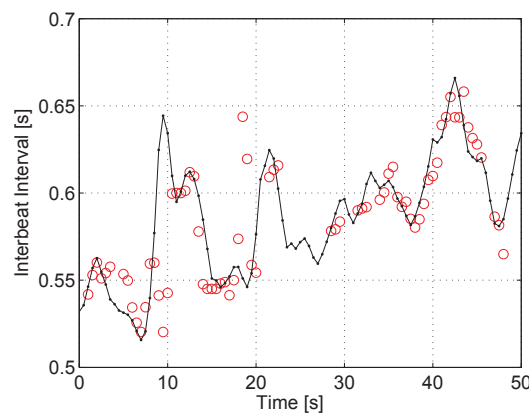

Fig. 21. Heart interbeat interval estimated from the output of the HPF and DCMP applied to $s_\mathrm{B}(t)$ when there is participant B only. The reference ECG data (black line) and radar measurement (red circles) are shown.
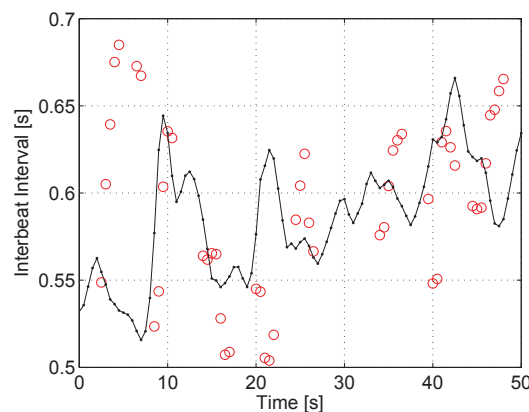

Fig. 22. Heart interbeat interval estimated from the output of the HPF applied to a single channel (ch1) of $s_\mathrm{A}(t) + s_\mathrm{B}(t)$ when there are both participants A and B. The reference ECG data (black line) and radar measurement (red circles) are shown.

(ch1) and the DCMP signals are 44.6 and 27.3 ms. When there are both participants A and B, the RMS errors of a single channel (ch1) and the DCMP signals are 64.4 and 20.9 ms. For both cases of a single participant and two participants, the use of the DCMP is shown to be effective in improving the accuracy of the estimation of the instantaneous heart rate. When applying the array beamforming to the signals from both participants in the scene, the RMS error in estimating the interbeat intervals is 53.4 ms, which is smaller than the error of the single channel, but larger than the error of the DCMP.

As stated above, the RMS errors in estimating the heart rate using the DCMP for a single participant and both participants are respectively 27.3 ms and 20.9 ms. We note that the latter is smaller than the former, which is counterintuitive. This can be explained by how the topology method works. As mentioned above, the topology method calculates the topological similarity between two adjacent waveforms, and if it is found to be low, the
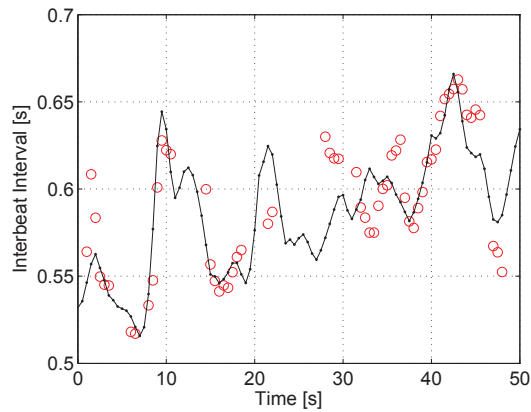
Fig. 23. Heart interbeat interval estimated using the proposed method from the output of the HPF and DCMP applied to $s_A(t) + s_B(t)$ when there are both participants A and B. The reference ECG data (black line) and radar measurement (red circles) are shown.
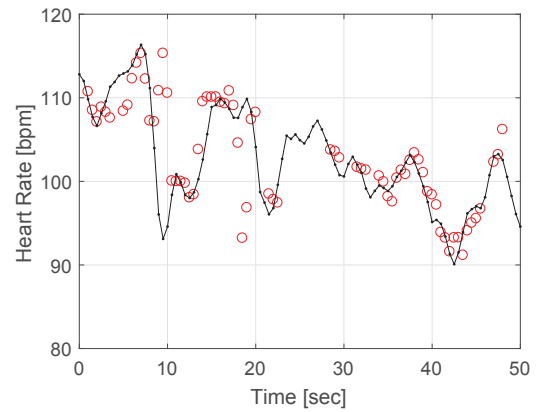

Fig. 25. Heart rate estimated from the output of the HPF and DCMP applied to $s_B(t)$ when there is participant B only. The reference ECG data (black line) and radar measurement (red circles) are shown.
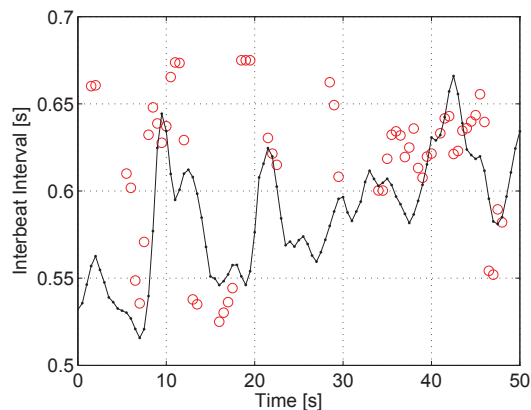

Fig. 24. Heart interbeat interval estimated from the output of the HPF and the conventional array beamforming applied to $s_A(t) + s_B(t)$ when there are both participants A and B. The reference ECG data (black line) and radar measurement (red circles) are shown.
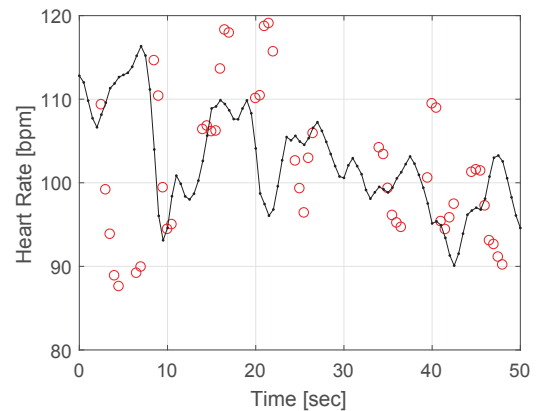

Fig. 26. Heart rate estimated from the output of the HPF applied to a single channel (ch1) of $s_A(t) + s_B(t)$ when there are both participants A and B. The reference ECG data (black line) and radar measurement (red circles) are shown.

unreliable heart rate estimate is eliminated. This is why we see some missing points in Figs. 21, 22 and 23. Therefore, a possible scenario is that when the desired echo is contaminated by interference, the topology algorithm detects waveform irregularity and eliminates more data points, resulting in a smaller RMS error.

To confirm this hypothesis, we define the success rate R_s as another measure of the performance in estimating the heart interbeat interval. The heart interbeat interval sequences measured using the ECG and radar are resampled every $\Delta t'$ and we obtain τ_n^{ECG} and τ_n^{radar} for $n = 1, 2, \cdots, N$, where $\Delta t' = 0.5$ s is selected considering the actual heart rate of participant B. We count the number of indices that satisfy a small error condition $|\tau_n^{ECG} - \tau_n^{radar}| < \tau_0$, where $\tau_0 = 50$ ms. The number of indices satisfying the condition is denoted N_0, and the success rate is obtained as $R_s = N_0/N$. The success rates R_s for participant B alone using a single channel and the DCMP were 52% and 68% while R_s for two participants

using a single channel and the DCMP were 32% and 59%. This result suggests that the seemingly low RMS error when two participants were measured using the DCMP was due to the lower success rate compared with the case of a single participant.

VIII. Discussion

A. Layout of Participants

In this paper, we demonstrated the measurement of the heart rate of a participant when two participants are located along the direction perpendicular to the line of sight. If participant B is located behind participant A, adaptive array processing alone cannot separate the echoes because the echoes arrive from the same direction. To separate echoes from the same direction, a wideband signal and a time-gating technique are needed instead of the narrowband signal used in the present study. In addition, the echo from participant B is likely to be blocked by participant A and the echo intensity will be
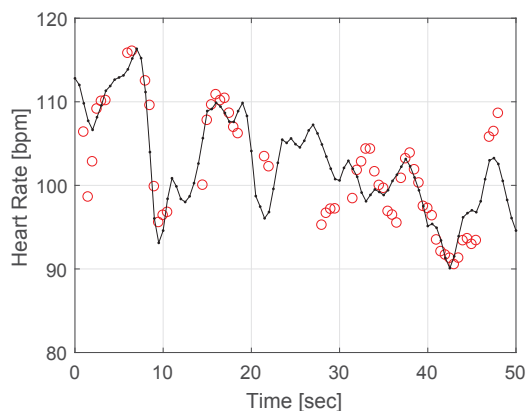
Fig. 27. Heart rate estimated using the proposed method from the output of the HPF and DCMP applied to $s_A(t) + s_B(t)$ when there are both participants A and B. The reference ECG data (black line) and radar measurement (red circles) are shown.
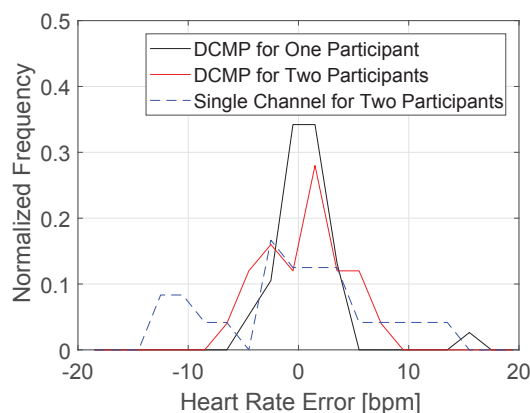

Fig. 28. Normalized histograms of errors in estimating the heart rate using the DCMP for one participant (black), DCMP for two participants (red), and a single channel for two participants (blue dashed).

too weak for detecting a tiny displacement associated with the heartbeat.

B. Sources of Error in the Heart Rate

In Fig. 22, we see a large discrepancy between the heart rates measured using the radar and ECG because the radar signal from a single channel is severely affected by the interfering echo from participant A. We also see some error in Fig. 23 because of imperfect suppression of the interference despite the use of an adaptive array. Because of the limited number of channels used for the measurement, the adaptive array processing was not able to completely suppress the interfering echo from participant A. Even in Fig. 21 for a single participant there is error in the estimation of the heart rate. This error can be caused by noise, interference and the physiological mechanism of the heartbeat measurement. Even when there is only a single participant in the scene, there are multiple body parts reflecting echoes that can interfere with the desired echo

containing vital signs. In addition, an ECG measures the electric activity of the heart, whereas the radar can only measure the mechanical activity. Although these electric and mechanical signals are closely related, they are not identical; the measurement of the instantaneous heart rate using radar is not necessarily identical to the reference instantaneous heart rate measured using an ECG.

C. Superposition of Echoes from Participants

In this paper, we synthesized an echo signal from two participants by superposing the separate signals measured for each of the participants. By measuring echoes separately and superposing the signals, we can compare the results for different scenarios with a single participant and multiple participants in the scene. Although measuring multiple participants simultaneously would provide the accuracy and error of the proposed method, it would be unclear where the error comes from; e.g. interference due to imperfect adaptive array processing or other reasons such as the limitation of the physiological measurement (i.e., the difference between the electro-cardiac signal and the mechanical cardiac vibration). Nonetheless, it will be an important study in future work to measure multiple participants simultaneously for the demonstration of the performance of the proposed method in a more realistic scenario.

IX. Conclusion

We proposed an adaptive-array-based approach for remote heartbeat measurements, which is capable of distinguishing the person of interest from other people in a multi-person environment. The method is based on a multi-channel X-band continuous-wave radar system and two types of adaptive array processing algorithms for vital sign processing. To verify the method, a dedicated demonstrator, which comprises planar wide-beam array antennas and a network analyzer, has been built and data for a multi-person scenario have been collected. The system can simultaneously measure four independent channels, and was used to make a four-element antenna-array measurement. We sequentially employed two adaptive array processing algorithms, the Capon method and a DCMP algorithm, to the measured signals and retrieved the desired radar signal from a subject of interest, while suppressing interfering clutter arriving from different directions. The proposed adaptive array approach was demonstrated to be efficient and improved the accuracy of the estimation of the human heart rate by a factor of 3.1 when there were two people standing next to each other.

References

[1] J.-M. Muñoz-Ferreras, Z. Peng, R. Gómez-García, and C. Li, "Review on advanced short-range multimode continuous-wave radar architectures for healthcare applications," IEEE Journal of Electromagnetics, RF and Microwaves in Medicine and Biology, vol. 1, no. 1, pp. 14–25, 2017.

[2] C. Li, Z. Peng, T.-Y. Huang, T. Fan, F.-K. Wang, T.-S. Horng, J.-M. Muñoz-Ferreras, R. Gómez-García, L. Ran, and J. Lin, "A review on recent progress of portable short-range noncontact microwave radar systems," IEEE Trans. Microw. Theory Techn., vol. 65, no. 5, pp. 1692–1706, 2017.

[3] A. D. Droitcour, O. Boric-Lubecke, V. M. Lubecke, J. Lin, G. T. A. Kovacs, "Range correlation and I/Q performance benefits in single-chip silicon Doppler radars for noncontact cardiopulmonary monitoring", IEEE Trans. Microw. Theory Techn., vol. 52, no. 3, pp. 838–848, 2004.

[4] C. Li, Y. Xiao, J. Lin, "Experiment and spectral analysis of a low-power Ka-band heartbeat detector measuring from four sides of a human body", IEEE Trans. Microw. Theory, vol. 54, no. 12, pp. 4464–4471, 2006.

[5] B.-K. Park, O. Boric-Lubecke, V. M. Lubecke, "Arctangent demodulation with DC offset compensation in quadrature Doppler radar receiver systems", IEEE Trans. Microw. Theory, vol. 55, no. 5, pp. 1073–1079, 2007.

[6] W. Massagram, V. M. Lubecke, A. Høst-Madsen, O. Boric-Lubecke, "Assessment of heart rate variability and respiratory sinus arrhythmia via Doppler radar", IEEE Trans. Microw. Theory, vol. 57, no. 10, pp. 2542–2549, 2009.

[7] D. Nagae, A. Mase, "Measurement of heart rate variability and stress evaluation by using microwave reflectometric vital signal sensing", Rev. Sci. Instrum., no. 81, pp. 094301, 2010.

[8] I. V. Mikhelson, S. Bakhtiari, T. W. Elmer II, A. V. Sahakian, "Remote sensing of heart rate and patterns of respiration on a stationary subject using 94-GHz millimeter-wave interferometry", IEEE Trans. Bio-med. Eng., vol. 58, no. 6, pp. 1671–1677, 2011.

[9] S. Bakhtiari, S. Liao, T. W. Elmer, N. S. Gopalsami, A. C. Raptis, "A real-time heart rate analysis for a remote millimeter wave I-Q sensor", IEEE Trans. Bio-med. Eng., vol. 5, no. 6, pp. 1839–1845, 2011.

[10] C. Lee, C. Yoon, H.-J. Kong, H. C. Kim, Y. Kim, "Heart rate tracking using a Doppler radar with the reassigned joint time-frequency transform", IEEE Antenn. Wirel. Pr., vol. 10, pp. 1096–1099, 2011.

[11] B. Schleicher, I. Nasr, A. Trasser, H. Schumacher, "IR-UWB radar demonstrator for ultra-fine movement detection and vital-sign monitoring", IEEE Trans. Microw. Theory Techn., vol. 61, no. 5, pp. 2076–2085, 2013.

[12] J. Kranjec, S. Begus, J. Drnovsek, G. Gersak, "Novel methods for noncontact heart rate measurement: a feasibility study", IEEE Trans. Instrum. Meas., vol. 63, no. 4, pp. 838–847, 2014.

[13] F. Adib, H. Mao, Z. Kabelac, D. Katabi, R. C. Miller, "Smart homes that monitor breathing and heart rate", Proc. Annual ACM Conference on Human Factors in Computing Systems, pp. 837–846, 2015.

[14] A. Vergara, N. Petrochilos, O. Boric-Lubecke, A. Host-Madsen, V. Lubecke, "Blind source separation of human body motion using direct conversion Doppler radar", IEEE MTT-S International Microwave Symposium Digest, pp. 1321–1324, 2008.

[15] I. V. Mikhelson, P. Lee, S. Bakhtiari, T. W. Elmer II, A. K. Katsaggelos, A. V. Sahakian, "Noncontact millimeter-wave real-time detection and tracking of heart rate on an ambulatory subject", IEEE Trans. Inf. Technol. B., vol. 16, no. 5, Sep. 2012.

[16] G. Wang, C. Gu, T. Inoue, C. Li, "A hybrid FMCW-interferometry radar for indoor precise positioning and versatile life activity monitoring", IEEE Transactions on Microwave Theory and Techniques, vol. 62, no. 11, pp. 2812–2822, 2014.

[17] C. Li, V. M. Lubecke, O. Boric-Lubecke, J. Lin, "A review on recent advances in Doppler radar sensors for noncontact healthcare monitoring", IEEE Transactions on Microwave Theory and Techniques, vol. 61, no. 5, pp. 2046–2060, 2013.

[18] Q. Zhou, J. Liu, A. Host-Madsen, O. Boric-Lubecke, V. Lubecke, "Detection of multiple heartbeats using Doppler radar", IEEE International Conference on Acoustics Speech and Signal Processing Proceedings, doi: 10.1109/ICASSP.2006.1660554, 2006.

[19] A. Boothby, V. Das, J. Lopez, J. Tsay, T. Nguyen, R. E. Banister, D. Y. C. Lie, "Accurate and continuous non-contact vital signs monitoring using phased array antennas in a clutter-free anechoic chamber", Proc. 35th Annual International Conference of the IEEE Engineering in Medicine and Biology Society, pp. 2862–2865, July 2013.

[20] T. Hall, B. T. Nukala, C. Stout, N. Brewer, J. Tsay, J. Lopez, R. E. Banister, T. Nguyen, D. Y. C. Lie, "A phased array non-contact vital signs sensor with automatic beam steering", Proc. IEEE MTT-S International Microwave Symposium, 2015.

[21] D. Samardzija, B.-K. Park, O. Boric-Lubecke, V. Lubecke, A. Host-Madsen, T. Sizer, "Experimental evaluation of multiple antenna techniques for remote sensing of physiological motion", Proc. IEEE/MTT-S International Microwave Symposium, doi: 10.1109/MWSYM.2007.380063, 2007.

[22] C.-Y. Hsu, C.-Y. Chuang, F.-K. Wang, T.-S. Horng, L.-T. Hwang, "Detection of vital signs for multiple subjects by using self-injection-locked radar and mutually injection-locked beam scanning array", Proc. 2017 International Microwave Symposium, no. WE2G-1, 2017.

[23] I. Mostafanezhad, E. Yavari, O. Boric-Lubecke, "A low cost simple RF front end using time-domain multiplexing for direction of arrival estimation of physiological signals", IEEE MTT-S International Microwave Symposium Digest, doi: 10.1109/MWSYM.2013.6697778, 2013.

[24] O. L. Frost, III, "An algorithm for linearly constrained adaptive array processing," Proc. IEEE, vol. 60, no. 8, 1972.

[25] K. Takao and N. Kikuma, "Tamed adaptive antenna array," IEEE Trans. Ant. & Propagt., vol. AP-34, no. 3, 1986.

[26] T. Sakamoto, R. Imasaka, H. Taki, T. Sato, M. Yoshioka, K. Inoue, T. Fukuda, H. Sakai, "Feature-based correlation and topological similarity for interbeat interval estimation using ultra-wideband radar", IEEE Trans. Bio-med. Eng., vol. 63, no. 4, pp. 747–757, 2016.

[27] T. Sakamoto, R. Imasaka, H. Taki, T. Sato, M. Yoshioka, K. Inoue, T. Fukuda, H. Sakai, "Accurate heartbeat monitoring using ultra-wideband radar", IEICE Electronics Express, vol. 12, no. 3, pp. 20141197, 2015.

[28] T. Sakamoto, S. Okumura, R. Imanishi, H. Taki, T. Sato, M. Yoshioka, K. Inoue, T. Fukuda, H. Sakai, "Remote heartbeat monitoring from human soles using 60-GHz ultra-wideband radar", IEICE Electronics Express, vol. 12, no. 21, pp. 20150786, 2015.

[29] T. Sakamoto, P. J. Aubry, A. G. Yarovoy, S. Okumura, H. Taki, T. Sato, "Super-resolution array radar imaging of human bodies for heartbeat monitoring", Proc. XXXIInd International Union of Radio Science General Assembly & Scientific Symposium, no. B35-1, 2017.

[30] S. E. Valavan, D. Tran, A. G. Yarovoy, A. G. Roederer, "Dual-band wide-angle scanning planar phased array in X/Ku-bands", IEEE Trans. Ant. Propagt., vol. 62, no. 5, pp. 2514–2521, 2014.

[31] S. E. Valavan, "Dual-band planar wide-angle scanning phased arrays", Doctoral dissertation, Delft University of Technology, 2014.

[32] M. Muragaki, S. Okumura, T. Sakamoto, T. Sato, "Non-contact respiration measurement using ultra-wideband array radar with adaptive beamforming technique for cancer radiotherapy", Proc. International Symposium on Antennas and Propagation, Oct. 2016.

[33] C. Li, J. Lin, "Optimal carrier frequency of non-contact vital sign detectors", IEEE Radio and Wireless Symposium, doi: 10.1109/RWS.2007.351823, 2007.

[34] M. Zakrzewski, H. Raittinen, J. Vanhala, "Comparison of center estimation algorithms for heart and respiration monitoring with microwave Doppler radar", IEEE Sens. J., vol. 12, no. 3, pp. 627–634, 2012.

[35] W. Hu, Z. Zhao, Y. Wang, H. Zhang, F. Lin, "Noncontact accurate measurement of cardiopulmonary activity using a compact quadrature Doppler radar sensor", IEEE Trans. Bio-med. Eng., vol. 61, no. 3, pp. 725–735, 2014.

[36] S. Okumura, T. Sakamoto, T. Sato, M. Yoshioka, K. Inoue, T. Fukuda, H. Sakai, "Comparison of clutter rejection techniques for measurement of small displacements of body surface using radar", Electronics Letters, DOI: 10.1049/el.2016.1461, 2016.

PLACE PHOTO HERE

Takuya Sakamoto (M'04-SM'17) received a B.E. degree in electrical and electronic engineering from Kyoto University, Kyoto, Japan, in 2000 and M.I. and Ph.D. degrees in communications and computer engineering from the Graduate School of Informatics, Kyoto University, in 2002 and 2005, respectively.

From 2006 through 2015, he was an Assistant Professor at the Graduate School of Informatics, Kyoto University. From 2011 through 2013, he was also a Visiting Researcher at Delft University of Technology, Delft, the Netherlands. Since 2015, he has been an Associate Professor at the Graduate School of Engineering, University of Hyogo, Himeji, Japan, and a Part-time Researcher with the Graduate School of Informatics, Kyoto University. In 2017, he was also a Visiting Scholar at University of Hawaii at Manoa, Honolulu, HI, USA. His current research interests lie in ultra-wideband radar, radar imaging, and radar signal processing.

Dr. Sakamoto was a recipient of the Best Paper Award from the International Symposium on Antennas and Propagation (ISAP) in 2004, the Young Researcher's Award from the Information and Communication Engineers of Japan (IEICE) in 2007, the Best Presentation Award from the Institute of Electrical Engineers of Japan (IEEJ) in 2007, the Best Paper Award from the IEICE Communication Society in 2007, the Best Paper Award from the ISAP in 2012, the Achievement Award from the IEICE Communications Society in 2015, and the Masao Horiba Award in 2016. In 2017, he was invited as a semi-plenary speaker of the European Conference on Antennas and Propagation (EuCAP) in Paris, France.

From 2015 until 2016, Dr. Sakamoto served as Treasurer of the IEEE Antennas and Propagation Society (AP-S) Kansai Joint Chapter and in 2017, he became its Secretary. Since 2016, he has also served as the Secretary of the IEICE Technical Committee on Electromagnetic Theory, an Associate Editor of IEICE Electronics Express, a Steering Committee Member of IEICE Kansai Section, and an Editorial Secretary for the IEICE Editorial Committee of Special Section. He convened a special session of the 2016 EuCAP in Davos, Switzerland.

PLACE PHOTO HERE

Pascal J. Aubry received the D.E.S.S. degree in electronics and automatics from the Université Pierre et Marie Curie (Paris 6), Paris, France, in 1993.

He was a Young Graduate Trainee with the European Space Research and Technology Centre (ESTEC) in 1996, where he was involved in antenna measurements. Since 1997, he has been with the International Research Centre for Telecommunications and Radar, Delft University of Technology (TUD), Delft, The Netherlands. His research interests include antenna measurement techniques, radar system testing, and signal processing and analysis.

PLACE PHOTO HERE

Shigeaki Okumura received his B.E. degree in electrical engineering from Kyoto University, Kyoto, Japan, in 2013 and M.I. degree in communications and computer engineering from the Graduate School of Informatics, Kyoto University, in 2015, where he is currently pursuing his Ph.D. degree. Since 2015, he has been a research fellow (DC1) of Japan Society for the Promotion of Science (JSPS). His current research interests include ultra-wideband radar imaging, medical ultrasound imaging, and signal processing.

PLACE PHOTO HERE

Hirofumi Taki received his M.D. and Ph.D. degrees in informatics from Kyoto University, Japan, in 2000 and 2007, respectively. He is currently Associate Professor of Graduate School of Biomedical Engineering at Tohoku University. His research interests include medical ultrasound, adaptive beamforming, and super-resolution imaging.

PLACE PHOTO HERE

Toru Sato (M'92) received his B.E., M.E., and Ph.D. degrees in electrical engineering from Kyoto University, Kyoto, Japan in 1976, 1978, and 1982, respectively. He has been with Kyoto University since 1983 and is currently a Professor in the Department of Communications and Computer Engineering, Graduate School of Informatics. His major research interests have include system design and signal processing aspects of UWB radars, atmospheric radars, radar remote sensing of the atmosphere, and biomedical imaging. Prof. Sato is a fellow of the Institute of Electronics, Information, and Communication Engineers of Japan, and a member of the Society of Geomagnetism and Earth, Planetary and Space Sciences, the Japan Society for Aeronautical and Space Sciences, the Institute of Electrical and Electronics Engineers, and American Meteorological Society.

PLACE PHOTO HERE

Alexander G. Yarovoy (F'15) graduated from the Kharkov State University, Ukraine, in 1984 with the Diploma with honor in radiophysics and electronics. He received the Candidate Phys. & Math. Sci. and Doctor Phys. & Math. Sci. degrees in radiophysics in 1987 and 1994, respectively.

In 1987 he joined the Department of Radiophysics at the Kharkov State University as a Researcher and became a Professor there in 1997. From September 1994 through 1996 he was with Technical University of Ilmenau, Germany as a Visiting Researcher. Since 1999 he is with the Delft University of Technology, the Netherlands. Since 2009 he leads there a chair of Microwave Sensing, Systems and Signals. His main research interests are in (ultra-)wideband radar, microwave imaging and applied electromagnetics (in particular, UWB antennas). He has authored and co-authored more than 450 scientific or technical papers, four patents and fourteen book chapters. He served as a Guest Editor of five special issues of the IEEE Transactions and other journals. Since 2011 he is an Associated Editor of the International Journal of Microwave and Wireless Technologies.

He is the recipient of the European Microwave Week Radar Award for the paper that best advances the state-of-the-art in radar technology in 2001 (together with L.P. Ligthart and P. van Genderen) and in 2012 (together with T. Savelyev). In 2010 together with D. Caratelli Prof. Yarovoy got the best paper award of the Applied Computational Electromagnetic Society (ACES).

Prof. Yarovoy served as the Chair and TPC chair of the 5th European Radar Conference (EuRAD'08), Amsterdam, the Netherlands, as well as the Secretary of the 1st European Radar Conference (EuRAD'04), Amsterdam, the Netherlands. Prof. Yarovoy served also as the co-chair and TPC chair of the Xth International Conference on GPR (GPR2004) in Delft, the Netherlands. From 2008 till 2017 he served as Director of the European Microwave Association (EuMA).